

36. Although the 3'-most residue of the RNA is in the position of a nucleotide just added to the chain, it must have undergone translocation and then returned to this position before crystallization. Translocation is necessary to create a site for the next nucleotide, whose absence from the reaction results in a paused complex.
37. G. M. Cheetham, T. A. Steitz, *Science* **286**, 2305 (1999).
38. Y. Tintut, J. T. Wang, J. D. Gralla, *J. Biol. Chem.* **270**, 24392 (1995).
39. L. Kinsella, C. Y. Hsu, W. Schulz, D. Dennis, *Biochemistry* **21**, 2719 (1982).
40. D. J. Jin, C. L. Turnbough, *J. Mol. Biol.* **236**, 72 (1994).
41. J. R. Levin, B. Krummel, M. J. Chamberlin, *J. Mol. Biol.* **196**, 85 (1987); B. Krummel, M. J. Chamberlin, *Biochemistry* **28**, 7829 (1989); F. C. P. Holstege, U. Fiedler, H. T. M. Timmers, *EMBO J.* **16**, 7468 (1997).
42. W. Gu, M. Wind, D. Reines, *Proc. Natl. Acad. Sci. U.S.A.* **93**, 6935 (1996).
43. Ordering of the rudder and lid may not be observed because of structural heterogeneity of the transcribing complexes in this region. Heterogeneity might be expected as a consequence of inefficient displacement of RNA from DNA-RNA hybrid during transcription of tailed templates.
44. S. S. Daube, P. H. von Hippel, *Science* **258**, 1320 (1992).
45. A. T. Brünger et al., *Acta Crystallogr. D* **54**, 905 (1998).
46. For assistance at beamlines 1-5, 7-1, 9-1, and 9-2 of the Stanford Synchrotron Radiation Laboratory (SSRL), we thank H. Bellamy, A. Cohen, P. Ellis, P. Kuhn, T. McPhillips, M. Soltis, and the other members of the SSRL user support staff. This research is based in part on work done at SSRL, which is funded by the U.S. Department of Energy (DOE) Office of Basic Energy Sciences. The structural biology program is supported by the NIH National Center for Research Resources Biomedical Technology Program and the DOE Office of Biological and Environmental Research. We thank COMPAQ for

providing a Unix workstation. We thank N. Thompson and R. Burgess for generously providing antibody for protein purification. We thank J. Puglisi and members of the Kornberg laboratory for comments on the manuscript. The contribution of A.L.G. was sponsored by USAMRMC Breast Cancer Initiative, DAMD17-97-7099, and does not necessarily reflect the policy of the government. P.C. was supported by a postdoctoral fellowship of the Deutsche Forschungsgemeinschaft (DFG). D.A.B. was supported by postdoctoral fellowship PF-00-014-01-GMC from the American Cancer Society. This research was supported by NIH grant GM49985 to R.D.K. Coordinates have been deposited at the Protein Data Bank (accession code 1I6H).

1 February 2001; accepted 28 March 2001

Published online 19 April 2001;

10.1126/science.1059495

Include this information when citing this paper.

## Evidence for Substantial Variations of Atmospheric Hydroxyl Radicals in the Past Two Decades

R. G. Prinn,<sup>1</sup> J. Huang,<sup>1</sup> R. F. Weiss,<sup>2</sup> D. M. Cunnold,<sup>3</sup> P. J. Fraser,<sup>4</sup> P. G. Simmonds,<sup>5</sup> A. McCulloch,<sup>5</sup> C. Harth,<sup>2</sup> P. Salameh,<sup>2</sup> S. O'Doherty,<sup>5</sup> R. H. J. Wang,<sup>3</sup> L. Porter,<sup>6</sup> B. R. Miller<sup>2</sup>

The hydroxyl radical (OH) is the dominant oxidizing chemical in the atmosphere. It destroys most air pollutants and many gases involved in ozone depletion and the greenhouse effect. Global measurements of 1,1,1-trichloroethane (CH<sub>3</sub>CCl<sub>3</sub>, methyl chloroform) provide an accurate method for determining the global and hemispheric behavior of OH. Measurements show that CH<sub>3</sub>CCl<sub>3</sub> levels rose steadily from 1978 to reach a maximum in 1992 and then decreased rapidly to levels in 2000 that were lower than the levels when measurements began in 1978. Analysis of these observations shows that global OH levels were growing between 1978 and 1988, but the growth rate was decreasing at a rate of  $0.23 \pm 0.18\%$  year<sup>-2</sup>, so that OH levels began declining after 1988. Overall, the global average OH trend between 1978 and 2000 was  $-0.64 \pm 0.60\%$  year<sup>-1</sup>. These variations imply important and unexpected gaps in current understanding of the capability of the atmosphere to cleanse itself.

The hydroxyl radical (OH) is the major oxidizing chemical in the lower atmosphere. The mole fractions and temporal trends of this very short-lived (~1 s) free radical are measurable at the local scale, but cannot presently be measured at the regional to global scale directly by in situ or remote sensing techniques. These

large-scale average mole fractions and trends can, however, be inferred indirectly from long-term global measurements of the trace gas 1,1,1-trichloroethane (CH<sub>3</sub>CCl<sub>3</sub>, methyl chloroform) because OH is the major destruction mechanism for this gas (1-5). Mole fractions of CH<sub>3</sub>CCl<sub>3</sub> have been measured continuously at several globally distributed stations from July 1978 to June 2000 in three sequential experiments: the Atmospheric Lifetime Experiment (ALE), the Global Atmospheric Gases Experiment (GAGE), and the Advanced Global Atmospheric Gases Experiment (AGAGE) (2, 6). These measurements can be combined with estimates of the emissions of CH<sub>3</sub>CCl<sub>3</sub> to determine concentrations and trends of OH after accounting for minor CH<sub>3</sub>CCl<sub>3</sub> removal mechanisms not involving OH (2). The derived OH concentrations then provide estimates of the

potentials for global warming and ozone depletion of a large number of anthropogenic chemicals (7-9).

### ALE, GAGE, and AGAGE Measurements

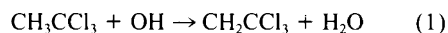
The ALE, GAGE, and AGAGE stations are located around the world at coastal sites that are generally remote from densely inhabited areas (10). Their locations were chosen to provide accurate measurements of the distributions and trends of trace gases whose lifetimes are long in comparison with global atmospheric circulation times. The air measurements are made in real-time with computer-controlled gas chromatographs that have packed columns and electron-capture detectors (6). Calibration is achieved by analysis (between air measurements) of an on-site cylinder of air that is calibrated in relation to parent standards before and after its use at each station (6).

The CH<sub>3</sub>CCl<sub>3</sub> mole fractions reported here are on the Scripps Institution of Oceanography SIO-1998 absolute calibration scale, which differs nonlinearly but slightly from the SIO-1993 scale used in our previous analysis (2, 5, 6). The scale has an estimated systematic accuracy of  $\pm 2\%$  (6). To account for possible errors in transferring the calibration to the earlier periods in the measurement record and possible past nonlinearity errors, we increased the uncertainty in absolute calibration of the actual measurements to  $\pm 5\%$  (2). The units for all CH<sub>3</sub>CCl<sub>3</sub> measurements reported here are dry-air mole fractions expressed as parts in 10<sup>12</sup> [parts per trillion (ppt)].

Monthly mean mole fractions ( $\chi$ ) and standard deviations ( $\sigma$ ) computed from the ~120 (ALE), 360 (GAGE), and 1080 (AGAGE) measurements made each month are shown in Fig. 1. Within each month, the actual high-frequency measurements reveal important short-term variations in mole fractions, including polluted air from nearby industrial regions (1, 5, 6). We omitted periods of obvious pollution in the calculation of  $\chi$  and  $\sigma$  to help ensure that they represent semi-hemispheric scales (5, 6).

<sup>1</sup>Department of Earth, Atmospheric, and Planetary Sciences, Massachusetts Institute of Technology, Cambridge, MA 02139, USA. <sup>2</sup>Scripps Institution of Oceanography, University of California, San Diego, La Jolla, CA 92093, USA. <sup>3</sup>Department of Earth and Atmospheric Sciences, Georgia Institute of Technology, Atlanta, GA 30332, USA. <sup>4</sup>Atmospheric Research, Commonwealth Scientific and Industrial Research Organization, Aspendale, Victoria 3195, Australia. <sup>5</sup>School of Chemistry, University of Bristol, Bristol BS8 1TH, UK. <sup>6</sup>Cape Grim Baseline Air Pollution Station, Bureau of Meteorology, Smithton, Tasmania 7330, Australia.

The observed magnitudes and recent decrease in the north-to-south differences and the annual cycles in  $\chi$  (Fig. 1) can be explained in terms of time variations and distances from sources (mainly Northern Hemisphere mid-latitude), the rate and seasonal variations in global circulation, and the seasonal variations in the rate of the major  $\text{CH}_3\text{CCl}_3$  destruction reaction



which has a local summer maximum (1). In addition, values of  $\chi$  at the Samoa station are sensitive to the El Niño–Southern Oscillation (ENSO) (1, 6).

The collapse of the north-south gradient in  $\chi$  is particularly dramatic following the time of maximum  $\chi$  values around 1992 (Fig. 1). This collapse (and of course the overall decreases in  $\chi$ ) is explained by the rapid decrease in  $\text{CH}_3\text{CCl}_3$  emissions in recent years caused by the regulation of this gas under the Montreal Protocol (6, 11).

#### OH Determination—Method

To deduce lifetimes ( $\tau$ ) and OH concentrations and trends, we use a recursive weighted least squares (Kalman) filter and a two-dimensional global model (2, 12). Estimates of unknowns contained in a (state) vector  $\mathbf{x}$  and their errors  $\epsilon$  contained in a (covariance) matrix  $\mathbf{P}$  are updated with

each new month of data using

$$\mathbf{x}(+) = \mathbf{x}(-) + \mathbf{K}(\mathbf{y}_0 - \mathbf{y}) \quad (2)$$

$$\mathbf{P}(+) = (1 - \mathbf{K}\mathbf{H})\mathbf{P}(-) \quad (3)$$

where the (gain) matrix  $\mathbf{K}$  is given by

$$\mathbf{K} = \mathbf{P}(-)\mathbf{H}^T[\mathbf{H}\mathbf{P}(-)\mathbf{H}^T + \mathbf{R}]^{-1} \quad (4)$$

Here,  $\mathbf{H}$  (and its transpose  $\mathbf{H}^T$ ) is a matrix containing the partial derivatives of the elements of the model-calculated values for  $\chi$  (contained in vector  $\mathbf{y}$ ) with respect to the elements of  $\mathbf{x}$ .  $\mathbf{H}$  is computed as a function of time with the same model used to calculate  $\mathbf{y}$ . The measurement (covariance) matrix  $\mathbf{R}$  is diagonal, with its elements being the variances ( $\sigma^2_k$ ) associated with the observed  $\chi$  values at station  $k$  (contained in vector  $\mathbf{y}_0$ ) augmented by an additional variance to account for model error (2, 12–15). The diagonal elements of the estimation error (covariance) matrix  $\mathbf{P}$  are the squares of the estimated errors  $\epsilon_i$  in the elements  $x_i$  of the state vector  $\mathbf{x}$ . The postscripts (–) and (+) denote values of  $\mathbf{P}$  and  $\mathbf{x}$  before and after use of each month's data.

Our global atmospheric model has 12 regions, with horizontal divisions at 90°N, 30°N, 0°, 30°S, and 90°S and vertical divisions at 1000, 500, 200, and 0 hPa (5). We define “reference” OH concentrations in the eight lower regions (16–24). The current best estimates of industrial  $\text{CH}_3\text{CCl}_3$  emissions and their uncertainties are input into the model (25–27).

Because our results are dependent on the trend in (as well as the magnitude of) the emissions, we also considered emissions for 1978 to 2000, which possess the maximum and minimum trends in this time period consistent with their  $2\sigma$  random errors (2). We did not include possible small emissions from biomass burning, vegetation, and soils in our best estimate emission scenario (5, 28, 29), but we do consider these emissions in our later error analysis.

We estimate OH concentrations and trends by multiplying the reference OH concentrations in the eight lower atmospheric boxes in our model by a dimensionless factor  $f = a + bP_1(t) + cP_2(t)$  to be determined. Here,  $P_n$  is a Legendre polynomial of order  $n$ ;  $t$  is time in years, measured from the midpoint (in 1989) of the 1978–2000 interval; and the unknown coefficients  $a$ ,  $b$ , and  $c$  are contained in the state vector  $\mathbf{x}$  and are optimally estimated with Eqs. 2 to 4 and each month's observations sequentially.

There are two other sinks for  $\text{CH}_3\text{CCl}_3$  included in the model besides reaction 1 in the eight lower atmospheric regions. Photochemical destruction of  $\text{CH}_3\text{CCl}_3$  occurs in the four upper atmospheric regions at rates specified from three stratospheric models (30). Also, loss to the ocean occurs in the four lowest atmospheric regions at rates obtained from oceanic observations (31, 32). These upper atmospheric and oceanic loss rates are considered known

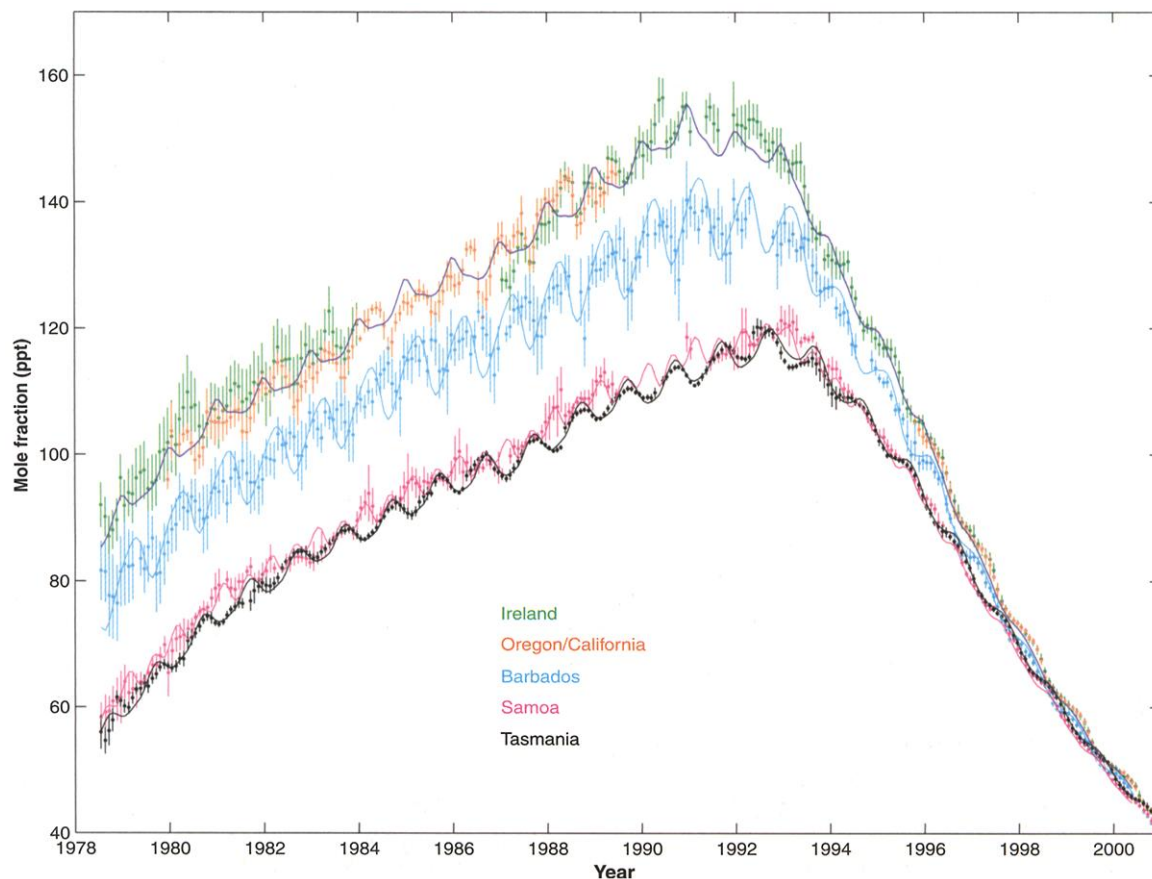


**Fig. 1.** ALE, GAGE, and AGAGE monthly mean mole fractions (dots) and standard deviations (error bars) for  $\text{CH}_3\text{CCl}_3$  from the five indicated stations. Also shown (solid curves) are the mole fractions computed in the model, with the optimally estimated OH distributions, and trends in both hemispheres, with the annualized content method. The time coordinate refers to the beginning of each year in this and in subsequent figures.

and are therefore not included in the state vector  $x$ . Because of a lack of quantitative estimates, we did not consider possible heterogeneous degradation of  $\text{CH}_3\text{CCl}_3$  on terrestrial clay minerals (33).

We determined  $a$ ,  $b$ , and  $c$  using three methods (2). The first method (content) estimates  $a$ ,  $b$ , and  $c$  and, because it assumes that the calibration is exact, it is sensitive to calibration error. The second method (annualized content) estimates  $f$  for each year's data individually.

These annual  $f$  values are then fit to the function  $a^* + b^*P_1(t) + c^*P_2(t)$  for comparison with the first method. The third method (trend) includes (along with  $a$ ,  $b$ , and  $c$ ) a dimensionless calibration coefficient  $\gamma$  of order unity in the state vector, which multiplies all  $\chi$  values and makes this method insensitive to absolute calibration errors, but sensitive to errors in percentage trends in  $\chi$ . All three methods are sensitive to emission and modeling errors.

Besides estimating a global value of  $f$ ,

we also estimated separate values of  $f$  for the Southern and Northern Hemispheres in the first two methods. Using these  $f$  values (global or hemispheric), we then calculated the time-averaged  $f$  (and hence time-averaged OH concentration), the time-averaged trend  $[(d \ln f)/dt = b/a \text{ year}^{-1}]$  in  $f$  (and hence in OH), and the time-averaged acceleration in the trend  $[(d^2 \ln f)/dt^2 = c/a \text{ year}^{-2}]$  in  $f$  (and hence in OH). We also used the estimated  $f$  values to correct the "reference" OH values in the model.

Given the environmental relevance of the absolute concentrations and trends in OH, the uncertainties in our OH estimates are very important. Errors ( $\epsilon_i$ ) in these estimates due to random measurement (instrumental and mismatch) errors ( $\sigma_k$ ) were automatically calculated in the inverse method as discussed earlier. Errors due to uncertainties in model parameters, emissions, and absolute calibration (34) were subsequently added to  $\epsilon_i$  and have been calculated with both sensitivity and Monte Carlo approaches (5).

**OH Determination—Results**

The optimally estimated time-averaged (1978–2000) OH concentrations, trends, and accelerations in these trends are summarized in Tables 1 and 2. The global weighted-average OH concentration,  $[9.4 \pm 1.3] \times 10^5 \text{ radicals cm}^{-3}$ , does not vary statistically from that derived by us earlier (2) from 1978–94 observations  $[(9.7 \pm 1.3) \times 10^5 \text{ cm}^{-3}$ , including rate constant error). The time-averaged OH trend  $(-0.64 \pm 0.60\% \text{ year}^{-1})$  does, however, differ from that reported earlier (2) for 1978–94  $(0.0 \pm 0.2\% \text{ year}^{-1})$  for three reasons. First, we are using improved estimates of emissions, which by themselves increase the estimated trend to  $\sim 0.3\% \text{ year}^{-1}$  for 1978–94 (25–27, 35, 36). Second, we see that the significant acceleration in the OH trend  $(-0.23 \pm 0.18\% \text{ year}^{-2})$  is negative over the full 1978–2000 time period, which means that the added data for 1994–2000 make the average trend much lower. Third, the small increase in the  $\text{CH}_3\text{CCl}_3$

**Table 1.** Optimal estimates of global and hemispheric weighted average OH concentrations (conc) ( $10^5$  radicals  $\text{cm}^{-3}$ ), OH trends (trend) ( $\% \text{ year}^{-1}$ ), and acceleration in OH trends (accel) ( $\% \text{ year}^{-2}$ ). Results are shown for the content (CON), annualized content (ACON), and trend (TREND) methods and for average concentrations, trends, and accelerations computed by combining two or three of these methods with equal weighting. The best estimates are considered to be a combination of the content and annualized content methods (39) (Table 2). The time-averaged total and process lifetimes (years) of  $\text{CH}_3\text{CCl}_3$  (using a combination of content and annualized content OH concentrations) are shown. Also shown are similarly defined lifetimes for  $\text{CH}_4$ . All uncertainties are  $1\sigma$ . Quoted errors are the average of the sensitivity and Monte Carlo error estimation methods (5, 34).

Parameter	Global	Northern Hemisphere	Southern Hemisphere
OH conc (CON)*	9.43 ± 1.30	8.98 ± 2.02	9.93 ± 2.02
OH trend (CON)	-0.66 ± 0.57	-0.51 ± 1.26	-0.91 ± 1.03
OH accel (CON)	-0.23 ± 0.18	-0.62 ± 0.38	+0.13 ± 0.12
OH conc (ACON)*	9.44 ± 1.25	8.88 ± 1.96	10.08 ± 1.98
OH trend (ACON)	-0.61 ± 0.56	-0.40 ± 1.28	-0.93 ± 1.01
OH accel (ACON)	-0.22 ± 0.17	-0.56 ± 0.35	+0.13 ± 0.10
OH conc (TREND)*	8.83 ± 1.11	7.96 ± 1.92	9.75 ± 1.70
OH conc (CON + ACON + TREND)*	9.23 <sup>+1.50</sup> <sub>-1.51</sub>	8.61 <sup>+2.39</sup> <sub>-2.57</sub>	9.92 <sup>+2.14</sup> <sub>-2.01</sub>
OH conc (CON + ACON)*	9.44 <sup>+1.30</sup> <sub>-1.31</sub>	8.93 <sup>+1.91</sup> <sub>-2.01</sub>	10.05 <sup>+2.06</sup> <sub>-2.10</sub>
OH trend (CON + ACON)	-0.64 <sup>+0.59</sup> <sub>-0.60</sub>	-0.46 <sup>+1.34</sup> <sub>-1.32</sub>	-0.92 <sup>+1.04</sup> <sub>-1.02</sub>
OH accel (CON + ACON)	-0.23 ± 0.18	-0.59 <sup>+0.38</sup> <sub>-0.41</sub>	+0.13 ± 0.12
$\text{CH}_3\text{CCl}_3$ lifetime (total)	4.90 <sup>+0.62</sup> <sub>-0.49</sub>	5.19 <sup>+1.17</sup> <sub>-0.77</sub>	4.58 <sup>+0.94</sup> <sub>-0.65</sub>
$\text{CH}_3\text{CCl}_3$ lifetime (tropospheric OH)	5.99 <sup>+0.95</sup> <sub>-0.71</sub>	6.32 <sup>+1.81</sup> <sub>-1.10</sub>	5.61 <sup>+1.45</sup> <sub>-0.93</sub>
$\text{CH}_3\text{CCl}_3$ lifetime (stratosphere)†	38.87 <sup>+0.34</sup> <sub>-0.32</sub>	41.03 <sup>+0.36</sup> <sub>-0.32</sub>	36.52 <sup>+0.75</sup> <sub>-0.69</sub>
$\text{CH}_3\text{CCl}_3$ lifetime (ocean)‡	89.01 <sup>+1.35</sup> <sub>-0.27</sub>	99.79 <sup>+0.21</sup> <sub>-0.23</sub>	79.17 <sup>+0.39</sup> <sub>-0.41</sub>
$\text{CH}_4$ lifetime (total)‡	9.27 <sup>+1.04</sup> <sub>-1.04</sub>	9.78 <sup>+2.53</sup> <sub>-1.60</sub>	8.71 <sup>+2.07</sup> <sub>-1.38</sub>
$\text{CH}_4$ lifetime (tropospheric OH)	10.12 <sup>+1.68</sup> <sub>-1.17</sub>	10.73 <sup>+3.11</sup> <sub>-1.84</sub>	9.48 <sup>+2.51</sup> <sub>-1.61</sub>
$\text{CH}_3$ lifetime (stratosphere)	109.6	111.4	107.8

\*Global and hemispheric averages weighted by air mass in each tropospheric model box. Averages weighted by  $\text{CH}_3\text{CCl}_3$  mass differ slightly from these [e.g.,  $9.32 \times 10^5 \text{ cm}^{-3}$  (CON),  $9.35 \times 10^5 \text{ cm}^{-3}$  (ACON),  $8.76 \times 10^5 \text{ cm}^{-3}$  (TREND), and  $9.14 \times 10^5 \text{ cm}^{-3}$  (CON + ACON + TREND) for the global case]. †Quoted uncertainties in these lifetimes are due only to differing  $\text{CH}_3\text{CCl}_3$  concentrations associated with differing OH concentrations. ‡The change of  $\text{CH}_4$  total lifetime from that reported earlier (2) is due to the different mass distributions of  $\text{CH}_4$ , different distributions of OH, and different rate constants used here.

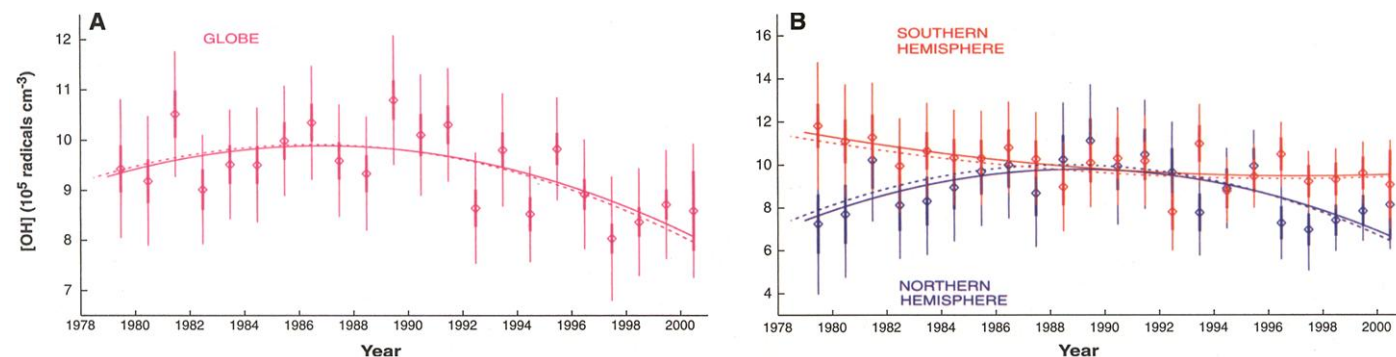


**Fig. 2.** Annual global (A) and hemispheric (B) OH concentrations estimated from the annualized content method with  $1\sigma$  error bars (thick for  $\epsilon_i$ , thin for total) estimated from the Kalman filter and Monte Carlo method (5, 34). For 2000, only six monthly running-mean observations are available, so  $\epsilon_i$

is larger. Also shown are polynomial fits to these annual concentrations (solid lines) and, for comparison, the best estimate polynomials determined with the content method (dashed lines). Trend accelerations represented by these polynomials are significantly nonzero (Table 1).

mole fractions due to the new calibration makes the trend slightly more positive (*I*).

On the average, over the 1978–2000 time period, the estimated Southern Hemispheric OH concentrations are  $\sim 14 \pm 35\%$  higher than the Northern Hemispheric values (Tables 1 and 2). This north-south asymmetry agrees qualitatively with some previous estimates, but not with others (2, 4, 5, 17–23, 37, 38). Related to this overall asymmetry are the OH trend accelerations, which are more negative in the Northern Hemisphere than in the Southern Hemisphere (Table 1).

In Fig. 2, we show the temporal variations in OH concentrations using the estimated *a*, *b*, and *c* values (content method) and *a\**, *b\**, and *c\** values (annualized content method) for the globe and Northern and Southern Hemispheres. We also show the actual year-by-year estimates of OH for the annualized content method. For this purpose, we use 12-month running means for  $\chi$  from both observations and model. The results with and without this smoothing are similar for *a\**, *b\**, and *c\**, but the annual OH estimates without the smoothing are more variable, as expected. The excellent agreement between the content (*a*, *b*, and *c*) and annualized content (*a\**, *b\**, and *c\**) methods for the global variations and the reasonable agreement for the hemispheric variations add credence to these

results (39). The global OH trend was positive from 1978 until about 1988 and then became increasingly negative after that. From Fig. 2, this global behavior is being substantially determined by the Northern Hemispheric behavior. There is a tendency for global OH levels to be lower in El Niño years, which may be real (e.g., associated with lowered ultraviolet fluxes due to increased equatorial cloud cover) or an artifact from the use of circulation parameters that do not account for the ENSO phenomenon.

To illustrate the overall uncertainty in our estimates, we show in Fig. 3 the probability distribution functions for these estimates calculated with the sensitivity and Monte Carlo methods (5). At the global level, the negative average linear trend is statistically significant and largely driven by the negative trend in OH in the Southern Hemisphere. The negative average acceleration in the global trend is also statistically significant, but is driven largely by the negative acceleration in the Northern Hemisphere (and opposed by the smaller positive acceleration in the Southern Hemisphere).

Using the estimated OH concentrations (Table 2), we also computed the “total” lifetime of  $\text{CH}_3\text{CCl}_3$ , defined as its total mass in the atmosphere divided by its total rate of destruction. We also computed three “process” lifetimes, defined as the total atmo-

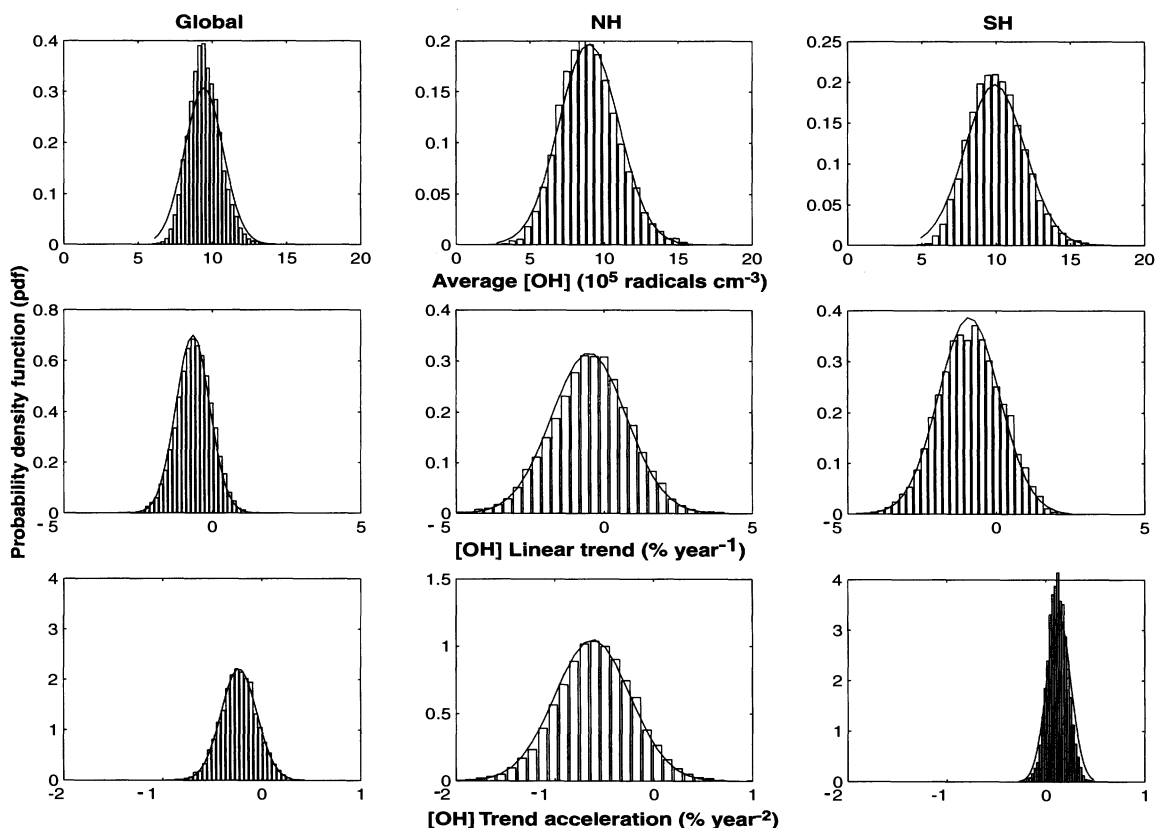
spheric mass of  $\text{CH}_3\text{CCl}_3$  divided by its rates of destruction due separately to OH in the lower atmosphere, photochemical reactions in the upper atmosphere (stratosphere), and oceanic uptake (Table 1). The sum of the inverses of these three process lifetimes equals the inverse of the total lifetime.

These OH and lifetime results have important implications for a large number of chemically and radiatively important trace gases, including methane ( $\text{CH}_4$ ). The lifetime for  $\text{CH}_4$  calculated here (Table 1) is not statistically different from that computed by us earlier [ $8.9^{+1.4}_{-1.1}$  years (2), including rate constant errors]. However, our estimated OH trends imply a time-varying lifetime for  $\text{CH}_4$ , which was decreasing up to 1988 and increasing substantially since then.

### Unmodeled Nonlinearity and Calibration Errors

To test these results, we performed a number of additional numerical experiments. Because the post-1997 measured mole fractions are below the lowest SIO-1998 AGAGE primary calibration standard (69 ppt), it is possible that the post-1997 extrapolations of these calibrations have introduced an uncorrected nonlinearity, producing a possible error of +0.3% or +0.15 ppt in 2000 (5). For comparison, we calculated the differences between the observed 12-month running mean  $\text{CH}_3\text{CCl}_3$   $\chi$  values and the  $\chi$

**Fig. 3.** Histograms showing probability distribution functions (pdfs) for global, Northern Hemispheric (NH), and Southern Hemispheric (SH) estimates of global average  $[\text{OH}]$  ( $10^5 \text{ cm}^{-3}$ ),  $100b/\hat{a}$  (OH trend in %/year), and  $100c/\hat{a}$  (acceleration in OH trend in  $\% \text{ year}^{-2}$ ), computed with the content and Monte Carlo (10,000 samples) methods. Here,  $\hat{a}$  is the best estimate of *a*. Shown for comparison (as solid lines) are the probability distribution functions computed from the standard deviations estimated with the sensitivity method, assuming normal (Gaussian) distributions. We emphasize that the three variables shown for the global case and the six variables shown for the Southern and Northern Hemispheric cases are related because each variable corresponds to a particular Monte Carlo model run.



values that would be required to yield time-invariant OH values (Fig. 4). These differences are much larger (e.g., up to +4 ppt or +10% in mid-2000) than could be explained by an uncorrected nonlinearity. To further address the possibility of nonlinearity in the recent AGAGE data, we repeated our OH estimations using the content method, but omitting the post-1997 data. We obtain  $[\text{OH}] = 9.59 \times 10^5 \text{ cm}^{-3}$ , trend =  $-0.34\% \text{ year}^{-1}$ , and trend acceleration =  $-0.23\% \text{ year}^{-2}$ , which do not differ significantly from their values in Table 1.

There are also differences in the absolute  $\text{CH}_3\text{CCl}_3$  calibration and trends measured by AGAGE and the National Oceanic and Atmospheric Administration (NOAA) (4–6). To examine the calibration differences, we simply adjusted our data to the NOAA absolute calibration scale (dividing by 0.945). Using the content method, we deduced  $[\text{OH}] = 8.9 \times 10^5 \text{ cm}^{-3}$ , trend =  $-0.20\% \text{ year}^{-1}$ , and trend acceleration =  $-0.20\% \text{ year}^{-2}$ , which are well within the ranges in Table 1. This dependence of the trend on calibration is theoretically expected (1,

2). To examine  $\text{CH}_3\text{CCl}_3$  trend differences, we replaced our 1994–2000  $\chi$  values with average values from the NOAA stations in the four semi-hemispheres (after multiplying them by 0.945 to place them on the AGAGE calibration scale). However, we retained the standard deviations from AGAGE because the NOAA flask data are too infrequent to define intramonthly variations. Using the content method, we obtained  $[\text{OH}] = 9.46 \times 10^5 \text{ cm}^{-3}$ , trend =  $-0.59\% \text{ per year}$ , and trend acceleration =  $-0.22\% \text{ year}^{-2}$ , which are all very similar to those values in Table 1.

Finally, after the removal of pollution from the data, our 30° to 90°N station data refer to background marine air and may therefore be underestimating  $\text{CH}_3\text{CCl}_3$  levels in this region whenever continental emissions are large. The magnitude of this underestimate would decrease as the  $\text{CH}_3\text{CCl}_3$  gradients, and hence the  $\sigma_k$  values, decreased in recent times. To assess this effect, we augmented the 30° to 90°N  $\text{CH}_3\text{CCl}_3$  values by 3 ppt multiplied by  $\sigma_k$  and divided by the maximum value of  $\sigma_k$  in the time

series. We obtained  $[\text{OH}] = 9.51 \times 10^5 \text{ cm}^{-3}$ , trend =  $-0.64\% \text{ year}^{-1}$ , and acceleration =  $-0.24\% \text{ year}^{-2}$ , using the content method; again, these values are not significantly different from the values in Table 1.

### Emissions for Zero Trend

Given the above results, it is of interest to determine optimally those emissions that would be consistent with a zero trend in OH for comparison to our assumed industry emissions. This alternative inverse problem has been solved by including the annual emissions in the state vector  $\mathbf{x}$  and by specifying  $[\text{OH}]$  to be constant at its time-averaged values in Table 2. The average ratio of these estimated emissions to the industry emissions for 1979–95 is  $0.99 \pm 0.04$  (or an absolute difference of  $-9.8 \pm 25.4 \text{ Gg year}^{-1}$ ), with the actual ratio ranging from 0.92 in 1989 to 1.06 in 1994. The 1989 value is outside the range defined by the estimated errors in emissions (5, 25–27). Even more telling, for the years 1996–2000, the ratios become 1.2, 2.0, 2.2, 1.7, and 1.7, respectively (or absolute differences of +17, +41, +29, +16, and +14  $\text{Gg year}^{-1}$ , respectively). If these differences are correct, then the phaseout of  $\text{CH}_3\text{CCl}_3$  consumption reported by the parties to the Montreal Protocol must be incorrect (11). These recent substantial differences are, however, far too large to be explained by estimates of emission errors (5, 25–27) or by our neglect of biomass burning and other nonindustrial emissions (5, 28, 29). Also, the biomass burning emissions are expected to be fairly uniform over time and not concentrated in 1996–2000. A strict upper limit on the total natural background sources of  $\text{CH}_3\text{CCl}_3$  of  $10 \text{ Gg year}^{-1}$  is set from analyses of air trapped in Antarctic firn ice (40–42). The simple addition of a constant  $10 \text{ Gg year}^{-1}$  emissions over 1951–2000 does not change the estimated OH trends and accelerations significantly. Also, the near cessation of significantly elevated  $\text{CH}_3\text{CCl}_3$  levels in polluted air sampled at the Tasmania, California, and Ireland stations (6) implies that total anthropogenic  $\text{CH}_3\text{CCl}_3$  emissions in 1999 from Australia, western North America, and Europe are less than a few gigagrams (5, 43). We therefore conclude that the emissions necessary to yield a zero trend in OH are unacceptable, particularly in the 1996–2000 time frame.

### Conclusions

Theoretical analysis of the  $\text{CH}_3\text{CCl}_3$  data from ALE, GAGE, and AGAGE indicates a weighted global average 1978–2000 OH concentration of  $[9.4 \pm 1.3] \times 10^5 \text{ radicals cm}^{-3}$  with concentrations that are  $14 \pm 35\%$  lower in the Northern Hemisphere than in the Southern Hemisphere. These estimated OH concentrations are averages for 1978–2000 and are weighted toward the tropical lower

**Table 2.** Optimal estimates of time-averaged (1978–2000) OH concentrations ( $10^5 \text{ radicals cm}^{-3}$ ) in the lower atmosphere using the average of the content and annualized content methods with separate estimations for the Northern and Southern Hemispheres.

Division	90° to 30°S	30°S to 0°	0° to 30°N	30° to 90°N
200 to 500 hPa	$5.72^{+1.17}_{-1.20}$	$13.23^{+2.71}_{-2.76}$	$11.32^{+2.43}_{-2.55}$	$5.20^{+1.11}_{-1.17}$
500 to 1000 hPa	$5.47^{+1.12}_{-1.14}$	$15.32^{+3.14}_{-3.20}$	$12.87^{+2.75}_{-2.90}$	$5.79^{+1.24}_{-1.30}$

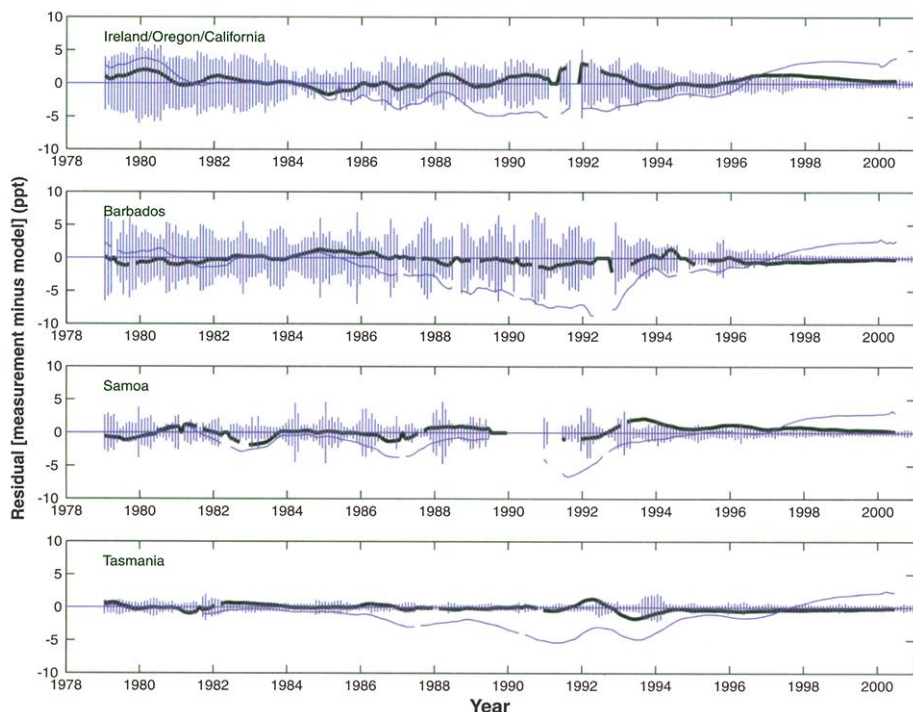


**Fig. 4.** Time variations in differences (residuals, in ppt) between  $\text{CH}_3\text{CCl}_3$  observations and (i) model predictions with the optimally estimated time-varying OH values in each hemisphere from the annualized content method (thick lines) and (ii) model predictions with the time-invariant optimally estimated OH values from a run of the content method, in which we estimate only the coefficient  $a$  in each hemisphere (thin lines). Vertical bars represent the monthly standard deviations ( $\chi$ ) in the observed monthly means.

time for  $\text{CH}_3\text{CCl}_3$  is  $4.9_{-0.5}^{+0.6}$  years, which is not statistically different from our previous estimate of  $4.8 \pm 0.3$  years (2).

From the annualized content method, global average OH levels rose  $15 \pm 22\%$  between 1979 and 1989 and then subsequently decreased to levels in 2000 about  $10 \pm 24\%$  below the 1979 values. From the content and annualized content methods (Table 1), negative acceleration in the global OH trend is dominated by changes in the Northern Hemisphere and suggests an anthropogenic cause for the major OH variations. The significance of the OH variations over time calculated here is amply demonstrated by the much better fit to the observations obtained in a model run with the time-varying OH from the annualized content method, as compared to a model run with constant OH (Fig. 4). A recent theoretical model study has concluded that OH should have a positive trend because of increases in air pollutant emissions (44). However, another recent study, which includes detailed consideration of the processing of these pollutant emissions at the urban scale, indicates that current models may be overestimating global  $\text{NO}_x$  and  $\text{O}_3$  levels from urban pollution and hence overestimating OH increases resulting from these pollutants (45). Several other model studies have concluded that OH has a negative trend between preindustrial and present times (23, 46–48). The recent negative OH trends reported here are not simply explained by the measured trends in trace gases involved in OH chemistry. There is no clear negative (or positive) global-scale trend in the major OH precursor gases,  $\text{O}_3$  and  $\text{NO}_x$ , between 1978 and 1999 (7–9). Levels of the dominant OH sink, CO, decreased rather than increased in the Northern Hemisphere between 1987 and 1998 (7–9). At the same time, concentrations of another important OH sink,  $\text{CH}_4$ , have risen significantly in the 1978–99 period (7–9). Perhaps increases in anthropogenic emissions in tropical and subtropical countries of short-lived trace gases, which react with OH (e.g., hydrocarbons and  $\text{SO}_2$ ), are involved. Also, a growth in levels of anthropogenic aerosols could increase heterogeneous OH destruction. Aerosol increases could also decrease OH production by lowering ultraviolet radiation fluxes through direct and indirect (via clouds) reflection and absorption. Neglect of these aerosols and urban-scale effects (45) in current models may also help to explain why OH levels are higher in the Southern Hemisphere than in the Northern Hemisphere, as deduced here. However, the identification of the exact cause of our reported OH variations will require further study. In this respect, the lack of long-term global-covering measurements of  $\text{O}_3$ ,  $\text{NO}_x$ ,  $\text{SO}_2$ , abundant hydrocarbons, and aerosols is a very substantial impediment to understanding

these changes in OH. If our current analysis is correct, it implies that the present understanding of OH chemistry, and hence of the capacity of the atmosphere to remove many anthropogenically and naturally produced trace gases, is incomplete. This has important implications for the mitigation of air pollution and climate change.

#### References and Notes

- R. G. Prinn et al., *J. Geophys. Res.* **97**, 2445 (1992).
- R. G. Prinn et al., *Science* **269**, 187 (1995).
- M. Krol, P. J. van Leeuwen, J. Lelieveld, *J. Geophys. Res.* **103**, 10697 (1998).
- S. Montzka et al., *Science* **288**, 500 (2000).
- Supplementary material is available at Science Online at [www.sciencemag.org/cgi/content/full/1058673/DC1](http://www.sciencemag.org/cgi/content/full/1058673/DC1).
- R. G. Prinn et al., *J. Geophys. Res.* **105**, 17751 (2000).
- M. J. Kurylo et al., in *Scientific Assessment of Ozone Depletion: 1998*, D. Albritton et al., Eds., Report 44 (World Meteorological Organization, Geneva, 1999), pp. 2.1–2.56.
- M. Prather et al., in *Climate Change 1995: The Science of Climate Change*, J. Houghton et al., Eds. (Cambridge Univ. Press, New York, 1996), pp. 86–103.
- D. Ehhalt et al., in *Climate Change 2001: The Science of Climate Change*, J. Houghton et al., Eds. (Cambridge Univ. Press, New York, in press).
- The ALE, GAGE, and AGAGE stations are located in five globally distributed sites: (i) Ireland, first at Adrigole,  $52^\circ\text{N}$ ,  $10^\circ\text{W}$  (1978–83), then at Mace Head,  $53^\circ\text{N}$ ,  $10^\circ\text{W}$  (1987 to present); (ii) U.S. West Coast, first at Cape Meares, Oregon,  $45^\circ\text{N}$ ,  $124^\circ\text{W}$  (1979–89), then at Trinidad Head, California,  $41^\circ\text{N}$ ,  $124^\circ\text{W}$  (1995 to present); (iii) Ragged Point, Barbados,  $13^\circ\text{N}$ ,  $59^\circ\text{W}$ , (1978 to present); (iv) Cape Matatula, American Samoa,  $14^\circ\text{S}$ ,  $171^\circ\text{W}$  (1978 to present); and (v) Cape Grim, Tasmania,  $41^\circ\text{S}$ ,  $145^\circ\text{E}$  (1978 to present).
- Handbook for the International Treaties for the Protection of the Ozone Layer* (United Nations Environment Programme, Nairobi, Kenya, ed. 4, 1996).
- R. G. Prinn, in *Inverse Methods in Global Biogeochemical Cycles*, P. Kasibhatla et al., Eds., vol. 114 of *Geophysical Monograph Series* (American Geophysical Union, Washington, DC, 2000), pp. 3–18.
- J. Huang, thesis, Massachusetts Institute of Technology (1999).
- D. M. Cunnold, R. G. Prinn, *J. Geophys. Res.* **96**, 17391 (1991).
- We use  $\sigma_k$  rather than the smaller instrumental precision error in defining  $R$  in order to account for the inability of the point measurements at the station to exactly determine the regional average  $\text{CH}_3\text{CCl}_3$  concentrations for comparison with our model, sometimes called “mismatch error” (12).
- Our reference OH concentrations and their uncertainties in each of the eight lower atmospheric regions are available (5) and are equated to the average and standard deviations of OH concentrations from six atmospheric models (17–23). We include a latitude-varying, solar-driven annual cycle in the OH concentrations. To compute  $\text{CH}_3\text{CCl}_3$  loss rates from these OH concentrations, we use the measured second-order rate constant and its uncertainty (24).
- A. Golombek, R. Prinn, *J. Atmos. Chem.* **16**, 179 (1993).
- A. R. Douglass, C. H. Jackman, R. S. Stolarski, *J. Geophys. Res.* **94**, 9862 (1989).
- C. H. Jackman, A. R. Douglass, R. B. Rood, R. D. McPeters, P. E. Meade, *J. Geophys. Res.* **95**, 7417 (1990).
- M. K. W. Ko, N. D. Sze, D. K. Weisenstein, *J. Geophys. Res.* **96**, 7547 (1991).
- M. G. Lawrence, P. J. Crutzen, P. J. Rasch, B. E. Eaton, N. M. Mahowald, *J. Geophys. Res.* **104**, 26245 (1999).
- C. M. Spivakovskiy et al., *J. Geophys. Res.* **105**, 8931 (2000).
- C. Wang, R. Prinn, A. Sokolov, *J. Geophys. Res.* **103**, 3399 (1998).
- W. B. DeMore et al., *Publication 97-4* (Jet Propulsion Laboratory, Pasadena, CA, 1997).
- P. M. Midgley, A. McCulloch, *Atmos. Environ.* **29**, 1601 (1995).
- A. McCulloch, P. M. Midgley, *Atmos. Environ.*, in press.
- Emissions are determined from global and regional sales and end-use data compiled using data from industry and, more recently, from consumption data collected in accordance with the Montreal Protocol (71, 25, 26). Uncertainty in these annual semi-hemispheric emissions is estimated on the basis of possible errors in production, sales, end-use assignments, and delay times for emissions after sales (25, 26). An error in the (9-month) delay time for end uses in the rapid release category of  $\pm 1$  month ( $1\sigma$ ) was added to the errors considered by Midgley and McCulloch (25). Overall errors are then determined by a Monte Carlo method. These errors are appropriately truncated if they imply unrealistic (e.g., negative) chemical stockpiles. The calculated global emissions and  $1\sigma$  errors, as well as the latitudinal distributions of these emissions, are available as supplemental Web material (5). Emissions rose from  $0.1_{-0.1}^{+0.0}$  Gg year $^{-1}$  in 1951 to a maximum of  $718 \pm 17.1$  Gg year $^{-1}$  in 1990 and then dropped to  $19.7_{-0.7}^{+0.6}$  Gg year $^{-1}$  in 2000.
- Global measurements imply a biomass burning source of  $\sim 5$  Gg year $^{-1}$  (29).
- J. Rudolph, K. von Czapiewski, R. Koppman, *Geophys. Res. Lett.* **27**, 1887 (2000).
- The assumed loss frequencies and their uncertainties in the four upper atmospheric (0 to 200 hPa) regions are available (5) and are defined from three models (17–20).
- The assumed global lifetime for oceanic loss (global amount divided by loss rate to ocean) is time variable with an assumed average of 89 years (32), and the loss rate is distributed in proportion to the oceanic area in each box. Our results are not significantly sensitive to alternative nonuniform distributions of this loss accounting for variations in surface temperature and exchange rates (5).
- J. H. Butler et al., *J. Geophys. Res.* **96**, 22347 (1991).
- S. Kutsuna, K. Takeuchi, T. Ibusuki, *J. Geophys. Res.* **105**, 6611 (2000).
- Modeling error estimates are deliberately very conservative and are considered for (i) model parameters (stratospheric-tropospheric vertical exchange times, tropospheric meridional exchange times, stratospheric chemical destruction times, tropospheric temperatures, tropospheric OH spatial distributions, oceanic removal times, and chemical rate constants), (ii) emissions (year-to-year and overall errors in annual industrial emissions, as well as industrial emission trend errors), and (iii) absolute calibration of measurements (2, 5, 13, 16, 24, 27). Among these, the largest source of error for  $b/a$  is calibration and for  $c/a$  is emissions trend. Because of the 23 years of measurements used in content methods, the contribution of  $\epsilon_i$  to the total error is very small compared to annualized content methods.
- For identical emissions, our analysis of 1978–94  $\text{CH}_3\text{CCl}_3$  data gives an OH trend of  $0.3\%$  year $^{-1}$ , whereas that of Krol et al. (3) yields  $0.46\%$  year $^{-1}$ . This difference lies well within the calculated uncertainty in the trends reported here. Possible reasons for this difference have been discussed (36).
- R. G. Prinn, J. Huang, *J. Geophys. Res.*, in press.
- S. Houweling, F. Dentener, J. Lelieveld, *J. Geophys. Res.* **103**, 10673 (1998).
- Y. Wang, J. Logan, D. Jacob, *J. Geophys. Res.* **103**, 10757 (1998).
- We reject the OH trends ( $b/a$ ) and accelerations ( $c/a$ ) from the trend method because this method produced a  $\gamma$  value of 1.1, which is well outside the allowable range ( $1.00 \pm 0.05$ ). Table 1 shows results from the trend method applied to the estimation of  $a$  and  $\gamma$  only, which yields  $\gamma = 1.07 \pm 0.08$  for both the global and Northern and Southern Hemisphere cases. The simultaneous estimation of  $\gamma$ ,  $a$ ,  $b$ , and  $c$  in the trend method is complicated by interrelationships between changes in  $\gamma$  and changes in the OH concentrations described by  $a$ ,  $b$ , and  $c$ , which make it more sensitive to errors than the content method.
- Butler et al. deduced that preindustrial  $\text{CH}_3\text{CCl}_3$  levels were  $< 1.5$  ppt (47). Similar measurements by Fraser

- (42) suggest that preindustrial levels were  $<1.9$  ppt. Assuming a steady state and a 4.9-year lifetime, these levels imply natural emissions of  $<10$  Gg year $^{-1}$ .
41. J. H. Butler *et al.*, *Nature* **399**, 749 (1999).
42. P. J. Fraser, unpublished data.
43. We estimate emissions of  $\sim 1$  Gg year $^{-1}$  in Europe in 1999, 0.06 Gg year $^{-1}$  in Australia in 1998–99, and  $<1$  Gg year $^{-1}$  in the western United States in 1999 (5).
44. S. Karlsdottir, I. S. A. Isaksen, *Geophys. Res. Lett.* **27**, 93 (2000).

45. M. Mayer, C. Wang, M. Webster, R. Prinn, *J. Geophys. Res.* **105**, 22869 (2000).
46. A. M. Thompson, *Science* **256**, 1157 (1992).
47. Y. Wang, D. Jacob, *J. Geophys. Res.* **103**, 31123 (1998).
48. P. J. Crutzen, P. H. Zimmerman, *Tellus* **43AB**, 136 (1991).
49. The ALE, GAGE, and AGAGE projects involved substantial efforts by many people beyond the authors of this paper (5). In its latest phase (AGAGE), support came (and comes) primarily from NASA, with important contribu-

tions from the Department of Environment, Transport and the Regions (United Kingdom); Commonwealth Scientific and Industrial Research Organization (Australia); Bureau of Meteorology (Australia); and NOAA, among others (5).

28 December 2000; accepted 17 April 2001

Published online 3 May 2001;

10.1126/science.1058673

Include this information when citing this paper.

## REPORTS

## New Ages for the Last Australian Megafauna: Continent-Wide Extinction About 46,000 Years Ago

Richard G. Roberts,<sup>1\*</sup> Timothy F. Flannery,<sup>2</sup> Linda K. Ayliffe,<sup>3†</sup> Hiroyuki Yoshida,<sup>1</sup> Jon M. Olley,<sup>4</sup> Gavin J. Prideaux,<sup>5</sup> Geoff M. Laslett,<sup>6</sup> Alexander Baynes,<sup>7</sup> M. A. Smith,<sup>8</sup> Rhys Jones,<sup>9</sup> Barton L. Smith<sup>10</sup>

All Australian land mammals, reptiles, and birds weighing more than 100 kilograms, and six of the seven genera with a body mass of 45 to 100 kilograms, perished in the late Quaternary. The timing and causes of these extinctions remain uncertain. We report burial ages for megafauna from 28 sites and infer extinction across the continent around 46,400 years ago (95% confidence interval, 51,200 to 39,800 years ago). Our results rule out extreme aridity at the Last Glacial Maximum as the cause of extinction, but not other climatic impacts; a "blitzkrieg" model of human-induced extinction; or an extended period of anthropogenic ecosystem disruption.

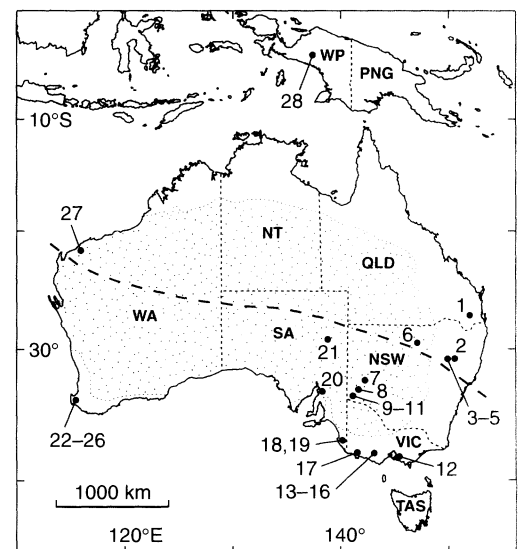
Twenty-three of the 24 genera of Australian land animals weighing more than 45 kg (which, along with a few smaller species, constituted the "megafauna") were extinct by the late Quaternary (1–3). The timing and causes of this environmental catastrophe have been debated for more than a century (4, 5), with megafaunal extirpation being attributed

to the impact of the first human colonizers (1, 5–8), who arrived  $56 \pm 4$  thousand years ago (ka) (9–13), or climate change (4) [in partic-

ular, increased aridity at the Last Glacial Maximum (19 to 23 ka) (14)]. A resolution to this debate has been thwarted by the lack of reliable ages for megafaunal remains and for the deposits containing these fossils. The disappearance of one species of giant bird (*Genyornis newtoni*) from the arid and semi-arid regions of southeastern Australia has been dated to  $50 \pm 5$  ka, on the basis of  $>700$  samples of eggshell (8), but no secure ages for extinction have been reported for the giant marsupials or reptiles, which constitute 22 of the 23 extinct genera of megafauna weighing  $>45$  kg. Here we present burial ages, obtained using optical and  $^{230}\text{Th}/^{234}\text{U}$  dating methods, for the remains of several megafaunal taxa (mostly giant marsupials; see Table 1) discovered at sites located in the humid coastal fringe and drier continental interior of Australia and in the montane forest of West Papua (Fig. 1), which was joined to Australia by a land bridge at times of lowered global sea level.

Most major biogeographic and climatic regions, and all five main groups of fossil sites (14), are represented in our survey. Most of the sites in southwestern Australia are caves that have acted as pitfall traps.

**Fig. 1.** Map of the Australian region showing the megafauna sites dated in this study. Site numbers: 1, Ned's Gully; 2, Mooki River; 3, Cox's Creek (Bando); 4, Cox's Creek (Kenloi); 5, Tambar Springs; 6, Cuddie Springs; 7, Lake Menindee (Sunset Strip); 8, Willow Point; 9, Lake Victoria (site 50); 10, Lake Victoria (site 51); 11, Lake Victoria (site 73); 12, Montford's Beach; 13, Lake Weering; 14, Lake Corangamite; 15, Lake Weeranganuk; 16, Lake Colongulac; 17, Warrnambool; 18, Victoria Fossil Cave (Grant Hall); 19, Victoria Fossil Cave (Fossil Chamber); 20, Wood Point; 21, Lake Callabonna; 22, Devil's Lair; 23, Kudjal Yolgha Cave; 24, Mammoth Cave; 25, Moondyne Cave; 26, Tight Entrance Cave; 27, Du Boulay Creek; 28, Kelangur Cave. The bold dashed line crossing the continent indicates the approximate present-day boundary between the zones dominated by summer rainfall from monsoonal activity (north of the line) and winter rainfall from westerly storm tracks (south of the line). The stippled area indicates the zone that receives less than 500 mm rainfall per year and where potential evapotranspiration exceeds mean monthly evapotranspiration year-round with negligible runoff. Climatic data are from (24, 38) and references therein.



<sup>1</sup>School of Earth Sciences, University of Melbourne, Melbourne, Victoria 3010, Australia. <sup>2</sup>South Australian Museum, Adelaide, South Australia 5000, Australia. <sup>3</sup>Laboratoire des Sciences du Climat et de l'Environnement, 91198 Gif-sur-Yvette, France. <sup>4</sup>Commonwealth Scientific and Industrial Research Organization (CSIRO) Land and Water, Canberra, ACT 2601, Australia. <sup>5</sup>Department of Earth Sciences, University of California, Riverside, CA 92521, USA. <sup>6</sup>CSIRO Mathematical and Information Sciences, Melbourne, Victoria 3168, Australia. <sup>7</sup>Western Australian Museum, Perth, Western Australia 6000, Australia. <sup>8</sup>National Museum of Australia, Canberra, ACT 2601, Australia. <sup>9</sup>Department of Archaeology and Natural History, Research School of Pacific and Asian Studies, Australian National University, Canberra, ACT 0200, Australia. <sup>10</sup>Department of Earth Sciences, La Trobe University, Melbourne, Victoria 3086, Australia.

\*To whom correspondence should be addressed. E-mail: rgrobe@unimelb.edu.au

†Present address: Department of Geology and Geophysics, University of Utah, Salt Lake City, UT 84112, USA.